Heliyon 9 (2023) e13871

Contents lists available at ScienceDirect

Heliyon

journal homepage: www.cell.com/heliyon

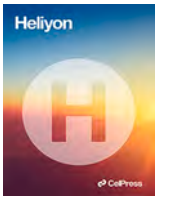

Research article

# Temperature-driven micro-fracturing in granite: The interplay between microstructure, mineralogy and tensile strength

T. Alcock [a], D. Bullen [b], P.M. Benson [b], S. Vinciguerra [a,*]

[a] Department of Earth Sciences, University of Turin, Italy
[b] Rock Mechanics Laboratory, School of Earth and Environmental Sciences, University of Portsmouth, UK

ARTICLE INFO

*Keywords:*
Devon Granite
Thermal treatment
Brazil tensile strength
Fracture density

ABSTRACT

High temperatures exert a significant influence on the mechanical and fluid flow properties of rocks and minerals. In crystalline rocks, differential thermal expansion of minerals is known to induce microfracture damage leading to changes in bulk volume and tensile strength. Here we report new data from thermally treated core samples of Devon Granite in order to constrain the interplay between tensile strength and thermally-induced damage with respect to the background mineralogy. A series of core samples was cyclically heated at temperatures ranging from 25 to 800 °C, with P-wave velocity and porosity measured after each cycle. Tensile strength decreased significantly from 9 MPa to less than 3 MPa as thermal treatment increased from 25 to 800 °C. The mechanical data were then compared to fracture density values obtained by optical maps of microfracture damage to assess the quantity and degree of linkage of intergranular and intragranular fractures using the FraqPaQ toolbox. The fracture density increased from 0.02 $mm^{-2}$ to 2.0 $mm^{-2}$ which is consistent with results obtained from direct physical parameters as calculated from elastic wave data. We conclude that the combined effects of thermal expansion and the $\alpha - \beta$ phase transition within quartz crystals has a pronounced effect on tensile strength.

## 1. Introduction

High temperature gradients are common in the Earth's crust, established across a wide range of local, regional and tectonic scales [1–6]. The resulting elevated gradients affect large crustal volumes giving rise to high-temperatures at relatively shallow depths typical of volcanic and geothermal systems which can alter the physical and mechanical behaviour of exposed rocks [7–10]. Granites and granitoids compose 20% of the continental crust and their physical and mechanical properties are particular sensitive to high temperatures, inducing mechanisms such as fatigue failure due to thermal strain within intergranular bonding [11,12]. This is particularly prominent in the temperature range 200 °C–600 °C [13,14]. This is reflected, for example, in the change in compressional and tensile strength and via Young's Modulus with decreases in stiffness [7,12]. Gautem et al. [15] presented data from Jalore Granite where increasing temperature from 25 °C to 200 °C initially led to an increase in tensile strength from 8.9 MPa to 9.9 MPa. However, as thermal stressing temperatures increased beyond 500 °C, a significant reduction in tensile strength to 1.4 MPa occurred. This behaviour is typical in crystalline rocks that have undergone thermal stressing due to the onset of the $\alpha - \beta$ phase transition of quartz and the oxidation of accessory minerals [15,16].

The relationship between tensile strength and thermally-induced fracturing has been linked to induced crack damage in the host

* Corresponding author.
*E-mail address:* sergiocarmelo.vinciguerra@unito.it (S. Vinciguerra).

https://doi.org/10.1016/j.heliyon.2023.e13871
Received 15 September 2022; Received in revised form 11 February 2023; Accepted 14 February 2023
Available online 18 February 2023

matrix, resulting in a significant reduction in the tensile strength [17,18]. This, in turn, decreases the fracture toughness as seen by mapping the evolving microstructure, for example in Westerly granite (Rhode Island), in terms of mineral contact and orientation. The overall effect is that a small increase in temperature may have a rapid and large increase in microfracture density (from 1.4 $mm/mm^{-2}$ at room temperature to 6.6 $mm/mm^{-2}$ at 850 °C) [19]. This behaviour was also noted by Griffiths et al. [20] who found that the number of fractures per unit area increased from 80 $mm^{-2}$ to 166 $mm^{-2}$ as the porosity of Garibaldi Grey Granite increased from less than 1%–3% due to thermal stressing. Similarly, Chen et al. [21] determined that Beishan Granite showed a significant increase in both intergranular and intragranular fracturing when thermally treated to above 500 °C, with porosity increasing from an initial value of less than 1%, to over 5% at 700 °C. This general behaviour has been reported by a number of authors who link thermal stressing to macroscopic rock physics data, including differential thermal expansion in the mineral assemblage and mineral phase transitions [11,20,22,23].

Petrological influences of thermal stressing have been examined using X-ray diffraction, such as in phyllosilicate structures which become more stable between 400 °C and 600 °C, with dehydroxylation occurring at approximately 400 °C [24]. This was mirrored by a decrease of the unconfined compressive strength and more ductile mechanical behaviour. Here we report a new laboratory data where the evolution of tensile strength and physical and mechanical properties were measured as a function of increasing thermal stress from 200° to 800 °C for a granite representative of the southwest of the UK. We particularly focus on how thermal treatment changes the physical and mechanical properties of the granite and the underlying petrological (mineralogical) controls via a systematic microstructural analysis of fracture propagation and damage. As well as analysing these data in terms of decreased physical and mechanical properties, we also make use of new rock physics toolkits to map out the microstructural observations with respect to microfracture density [25]. We use this method to quantitatively assess how the temperature-dependent fracturing is influenced by the background rock mineralogy.

## 2. Sample material and experimental procedure

The rock used is a coarse-grained granite sourced from the Cornubian Batholith around Dartmoor in Devon, United Kingdom. Prior to thermal treatment, a microstructural assessment was performed on the granite (Table 1) and it was found to be in line with previous mineralogical assessments [26,27]. Untreated granite consists primarily of quartz displaying sutured and serrated boundaries with patchy and sweeping extinction (Fig. 1), together with blocky, well-developed plagioclase and K-feldspars, (orthoclase and microcline). These occur as simple-twinned perthites or as small interstitial crystals, which also display patchy extinction in places. Muscovite and biotite mica occur as independent crystals, sometimes slightly bent, with aggregates of fine-grained muscovite being present on the edges of larger muscovite crystals. Both micas display noticeable traces of the basal cleavage and also exhibit sweeping extinction. The granite is fractured from previous deformation during late-stage Permian orogenesis. This occurs in the form of intergranular and intragranular microfractures along crystal grain boundaries and cleavage and twin planes in the micas and feldspars before they crosscut into quartz crystals [26,27].

Samples were initially cored into right cylinders of 40 mm diameter x 100 mm length. These were mounted inside a stainless-steel jig as described in Castagna et al. [28] and mounted into a Carbolite Tube Furnace (Fig. 2a) capable of 1200 °C. Samples were thermally treated to temperatures between 200 and 800 °C in steps of 100–200 °C (Table 2) where the target temperature was set at a ramp of 2 °C per minute followed by a dwell time of 30 min. This was done to ensure intergranular and intragranular fracturing would be initiated around and within crystals, and was followed by non-regulated cooling at a maximum of 2 °C per minute or more, dictated by the natural cooling rate. A thermocouple placed on the inside, near the sample, monitored and recorded the temperature throughout the process. Two untreated core samples acted as control specimens.

Thermally-treated samples were characterised by porosity, density and elastic P-wave velocity measurements. Velocities were measured using a Wavesurfer 3022 oscilloscope via the time-of flight method [29]. To determine density and porosity, sample volume and mass comparisons were made between dry and vacuum saturated samples, as per the standard ISRM method [30]. The determination of physical properties provided a proxy for the level of internal fracture damage at each temperature step, including the control specimens (Table 2). Each of the thermally-treated cores (200, 400, 600, 700 and 800 °C) were then sliced into 40 × 20 mm thick disks to be used for indirect tensile measurement via standard ISRM indirect Brazilian Disc test method (Fig. 2b) [31]. Three to five samples were tested at each thermal stressing temperature and the results averaged.

Detailed microstructural characterisation was conducted on thin sections of the granite samples at each thermal treatment stage using a Lecia M420 microscope. Photomicrographs were then produced and analyzed using FracPaQ. Analysis discarded those microfractures not related to thermal treatment and focused on microfracturing that was initiated and propagated at stress concentrators such as grain boundaries [11,32–34].. Fractures were drawn manually, taking into consideration geometry, density and aspect ratio as inputs for the FracPaQ calculation. These consisted of fracture patterns pre-processed as 8-bit grayscale.jpeg format photographs. The FracPaQ toolbox was then used to generate statistical analyses, using the Mauldon et al. [35] circular scanline sampling

**Table 1**
Mineral composition of Devon granite.

| | Mineral Proportions (%) | | | | | |
|---|---|---|---|---|---|---|
| | Quartz | K-Feldspar | Plagioclase | Biotite Mica | Muscovite Mica | Others |
| Devon Granite | 40 | 30 | 20 | 5 | 5 | 1> |

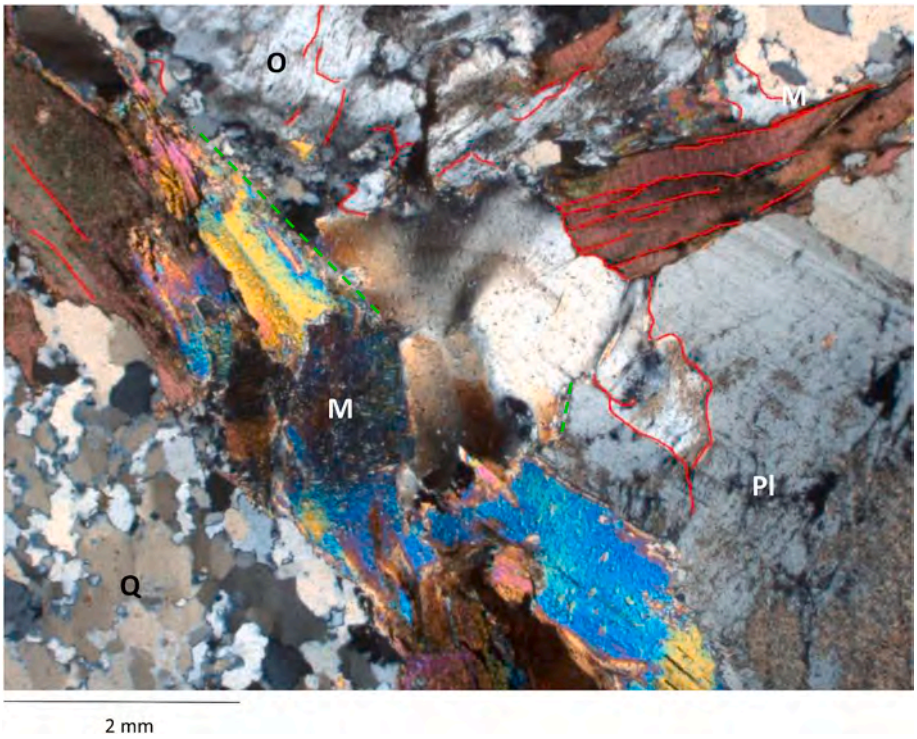


**Fig. 1.** Untreated Devon granite showing sub grain development in quartz (Q), fracturing (Red) along cleavage traces in muscovite mica crystals (M) and in microclines of orthoclase feldspar (O) and plagioclase feldspar (Pl) as well as the fine development of muscovite fringes (Green). (For interpretation of the references to colour in this figure legend, the reader is referred to the Web version of this article.)

method. Fracture density, defined as the number fractures per unit area, was determined using the number of intersections between fracture outlines in a circular radius, and the number of trace endpoints in a circular window, respectively. Average fracture trace lengths, defined as the average length of fractures from each circular window, were also calculated in each image analysis area.

## 3. Results

### 3.1. Laboratory data

Changes in sample density with temperature are shown in Fig. 3 and Table 2. The initial density of untreated granite is approximately 2.63 g/ $cm^3$. As thermal stress increases, density decreases by approximately 0.1 g/$cm^3$ at the maximum thermal stress of 800 °C, with a more pronounced decrease (2.58 g/$cm^3$ to 2.53 g/$cm^3$) between 700 °C and 800 °C. Changes in porosity with increasing temperature are more pronounced (Fig. 3). Initially, porosity of the untreated granite is low, approximately 0.2% (25 °C), increasing steadily up to a thermal stressing temperature of approximately 600 °C (1.6%) after which a rapid acceleration of porosity occurs to 2.7% at 700 °C and finally to 5.6% at 800 °C. Fig. 4 shows the decrease in P-wave elastic velocity with increasing thermal stress. Taken together, this implies that the mechanism is dominated by microfracture opening/growth, as porosity increases much faster than density decreases. This is further shown by the untreated P- wave velocity of the granite decreasing from 4.7 km/s to approximately 3.7 km/s at 400 °C, in a linear fashion. However, after this temperature the rate of decrease accelerates, to approximately 2 km/s at 700 °C and finally a significant decrease to just 0.5 km/s at 800 °C.

Results from the tensile strength experiments (Table 3) show an overall decrease with increasing thermal treatment (Fig. 5). However, on further inspection, the variation appears to show two distinct trends. At low thermal stressing temperature up to and including 400 °C, tensile strength decreases linearly from an average of 9 MPa on an untreated sample to an average of 6.8 MPa at 400 °*C* (a rate of decrease of 0.58 MPa per 100 °C). However, we note that the spread of values around the average at each temperature is large enough such that the decrease in strength from 25 °C to 400 °C is statistically very small. Above 400 °C, a more significant decrease in tensile strength is recorded from an average of 6.8 MPa to an average of 2.8 MPa at 600 °C (a rate of decrease of 2 MPa per 100 °C). The average tensile strength then remains within the range 2.2–2.9 (within sample variation) from 600 °C to 800 °C (Fig. 5, Table 3).

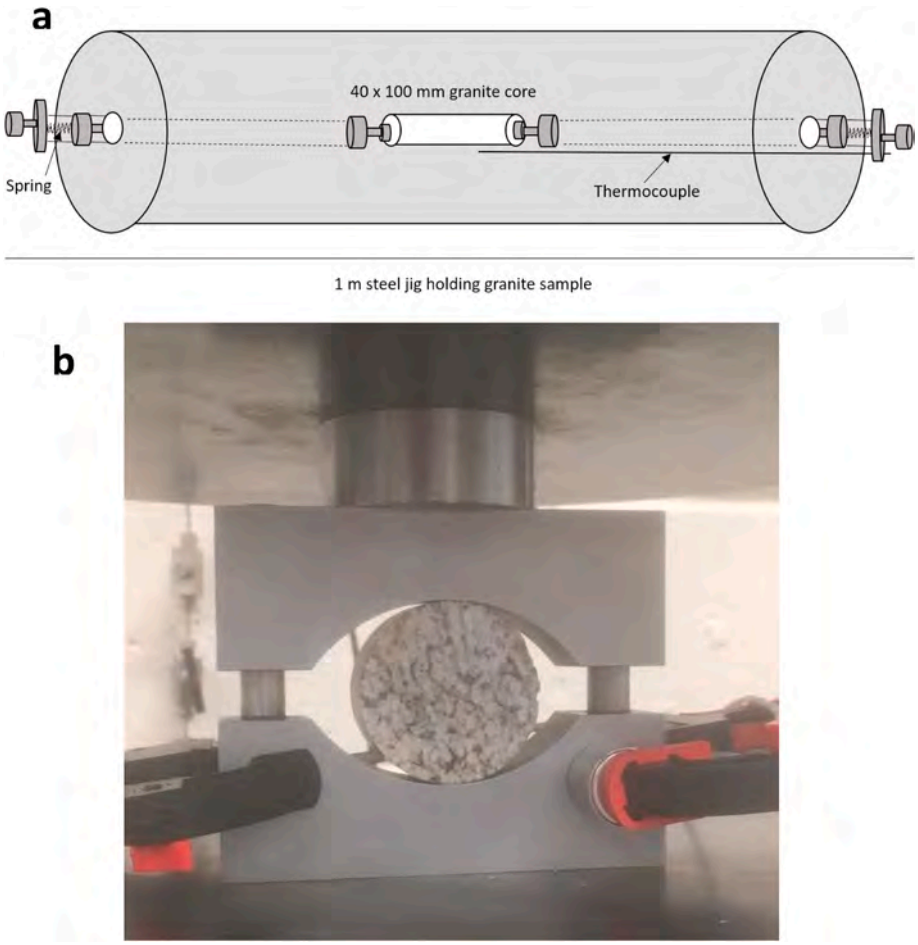


**Fig. 2.** Schematic view of Carbolite thermal treatment set up (a). The granite specimens were held in the centre of the furnace by a stainless-steel jig with springs that allowed the granite to expand and contract. Thermally treated granite during Brazil tensile strength (b). Stainless steel housing jaw held the granite in place while under an Instron hydraulic press.

**Table 2**
Physical properties of thermally-treated of Devon Granite core samples.

| Temperature (°C) | Density (g/cm$^3$) | P-wave velocity (km/s) | Porosity |
|---|---|---|---|
| 25 | 2.63 | 4.71 | 0.2 |
| 200 | 2.62 | 4.25 | 0.4 |
| 400 | 2.62 | 3.74 | 0.5 |
| 600 | 2.59 | 2.64 | 1.6 |
| 700 | 2.58 | 2.03 | 2.7 |
| 800 | 2.53 | 0.61 | 5.6 |

### 3.2. Microstructural observations

After thermal treatment, fracture characterisation was performed on the granite to assess mineralogical influences on micro-fracturing (Fig. 6a–e) with the latter dominating at the highest temperatures (Fig. 6d and e). Sub-grain development of quartz is noted, as well as the gradual expansion of feldspars with cleavage traces becoming more apparent in orthoclase from 400 °C (Fig. 6b) and then in plagioclase from 700 °C (Fig. 6d). The outward expansion of grains is noticeable from 600 °C, with intergranular and intragranular fractures becoming more common beyond 700 °C (Fig. 6d). Basal cleavage traces in muscovite and biotite also become more apparent with increasing temperature suggesting thermal expansion along these planes (Fig. 6c and d). Oxidation of biotite is evident from 600 °C with the mineral becoming opaque towards 800 °C (Fig. 6e).

A detailed investigation reveals that at 200 °C, there is already some evidence of structural control of fracture distribution with fractures following cleavage planes in muscovite, biotite, tourmalines and microclines (Fig. 6a). Larger microclines exhibited patchy

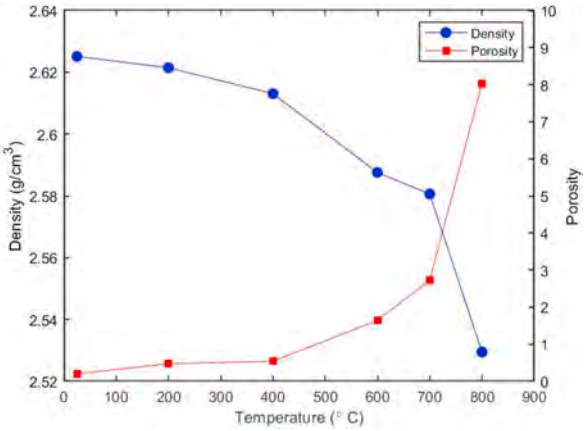


**Fig. 3.** Evolution of porosity and density of thermally treated Devon Granite from untreated to 800 °C.

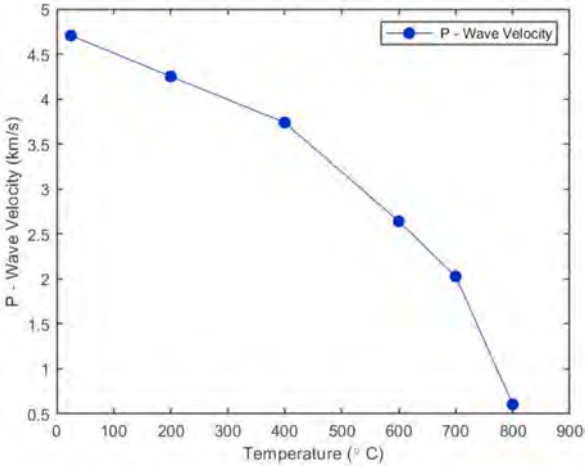


**Fig. 4.** Laboratory measured P-wave results of thermally treated Devon Granite from untreated to 800 °C.

**Table 3**
Tensile strength of thermally treated cores.

| Temperature (°C) | Number of Samples | Average Tensile Strength (MPa) | Rate of Change (MPa per 100 °C) |
|---|---|---|---|
| 25 | 4 | 9.03 | – |
| 200 | 4 | 7.98 | −1 |
| 400 | 4 | 6.84 | −1 |
| 600 | 3 | 2.84 | −2 |
| 700 | 4 | 2.17 | - 0.67 |
| 800 | 2 | 2.89 | 0.72 |

extinction and disrupted twinning. Minor discontinuous fractures have formed parallel to cleavage planes in plagioclase feldspar, and there are also evidences orthoclase crystals have fractures that follow perthites as opposed to cleavage. Microfractures start to develop in quartz passing from one sub-grain to another terminating along contacts with neighbouring quartz grains.

At 400 °C, there is continued sub-grain development in quartz, with fractures propagating along sub-grain boundaries. Fracturing within orthoclase continued to mimic the orientation of perthites (Fig. 6b). Both orthoclase and plagioclase feldspars display fractures parallel to cleavages. Fine-grained fringes are still present on muscovite grains, while random fractures begin to develop in tourmaline.

At 600 °C, there is further development of smaller sub-grains within quartz and fractures have become common around plagioclase-quartz and microcline-quartz margins (Fig. 6c). Fractures have developed between intergranular sub-grains of quartz then propagated through larger feldspar crystals before approximating the cleavage planes of plagioclase and muscovite. There is also evidence of fracturing in orthoclase crystals that approximates simple twinning, or follows sub-parallel to it, in addition to following zones of sericite. Furthermore, biotite has been oxidized to almost opaque material.

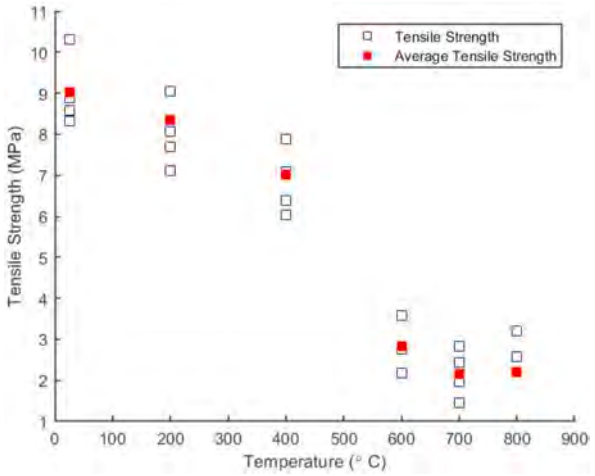


**Fig. 5.** Tensile strength and average tensile strength (red) of Devon granite samples after the thermal treatment process using the Brazil Tensile Test. (For interpretation of the references to colour in this figure legend, the reader is referred to the Web version of this article.)

At 700 °C, there are more visible intergranular fractures between quartz and plagioclase feldspars. Plagioclase showed some structural control on fractures with some crystals exhibiting bent twins, and fractures forming along cleavage planes (Fig. 6d). Large perthitic orthoclase contain fractures with limited structural control as suggested by the various fracture orientations. Microfractures extend from plagioclase and biotite inclusions within large orthoclase crystals. Here, microfractures pass from one inclusion to another along their respective grain margins. Biotite is further oxidized and has become near opaque whereas increased fracturing in tourmaline usually occurs as irregular transverse fractures due to poor cleavage development in this mineral.

Finally, at 800 °C, a visible fracture network consisting of both intergranular and intragranular fractures (Fig. 6e) has developed. Intragranular fractures form along the more defined basal cleavages of muscovite as well as mimicking perthites and twinning in feldspar crystals. Fractures have migrated around the intergranular boundary in their host grains, most notably around large felspar crystals before randomly passing through quartz sub-grains. Fractures in tourmaline increase in abundance, some of which connect to fractures that have formed along cleavage planes in neighbouring minerals.

### *3.3. Microfracture analysis*

In order to quantify the increasing damage induced by thermal treatment, we applied the FracPaQ toolbox (Fig. 7a–r) to quantify fracture patterns in thermally treated granite. The FracPaQ toolbox uses the Mauldon et al. [35], circular scanline method (Fig. 7g–l) to calculate the number of fractures, average fracture length and average fracture length in a predetermined area (e.g., 1 $mm^2$). The software is a reliable method to compare intergranular and intragranular fracturing (Fig. 8a–r) during each thermal treatment test (Fig. 9, Table 4) to show the evolution of fracturing with increasing temperature. FracPaQ determined 1228 intergranular fractures on the untreated samples, 2570 at 200 °C, 3017 at 400 °C, and 2789 at 600 °C. A large increase occurred between 600 °C and 700 °C with the number of fractures increasing by 118%–6085, and further increasing by 45%–8905 at 800 °C. The number of intragranular fractures followed a similar pattern: 889 fractures on the untreated samples, to 2147 at 200 °C, 2416 at 400 °C, and 3500 at 600 °C. Another large increase occurred at 700 °C with the number of intragranular fractures 123% higher at 7820 and increasing further by 28%–10,030 at 800 °C.

The FracPaQ-determined intergranular and intragranular fracture segment length remains similar within error until 600 °C (Table 4). At this temperature, intergranular fracture length decreased by 5% to 0.017 mm then by 9% to 0.015 mm at 700 °C remaining unchanged to 800 °C. Similarly, intragranular fracture length decreased by 8% to 0.016 mm at 600 °C and by a further 17% to 0.013 mm at 700 °C where it remained to 800 °C.

The increase in intergranular and intragranular fracture density (Fig. 10, Table 4) mirrors the decrease of fracture trace length with increasing temperature. The untreated intergranular fracture density is approximately 0.24 $mm^{-2}$. This then increases to 0.51 $mm^{-2}$ at 200 °C and between 200 °C and 600 °C further increases by 8% to 0.55 $mm^{-2}$. Above 600 °C, intergranular fracture density increases sharply by 62% to 0.89 $mm^{-2}$ at 700 °C, and then by a further 96% to 1.77 $mm^{-2}$ at 800 °C. Initial intragranular fracture density was calculated at 0.18 $mm^{-2}$. Intragranular fracture density then increases to 0.5 $mm^{-2}$. Between 200 °C and 600 °C, it increases by 40% to 0.69 $mm^{-2}$. The value increases significantly by 123% to 1.55 $mm^{-2}$ at 700 °C and further increases by 28% to 1.99 $mm^{-2}$ at 800 °C.

## 4. Discussion

Assessment of fracture density from direct image analysis has been combined with tensile strength and fracture damage derived from elastic wave velocity to understand the damage induced by increasing thermal stress on the mechanical properties of a granite

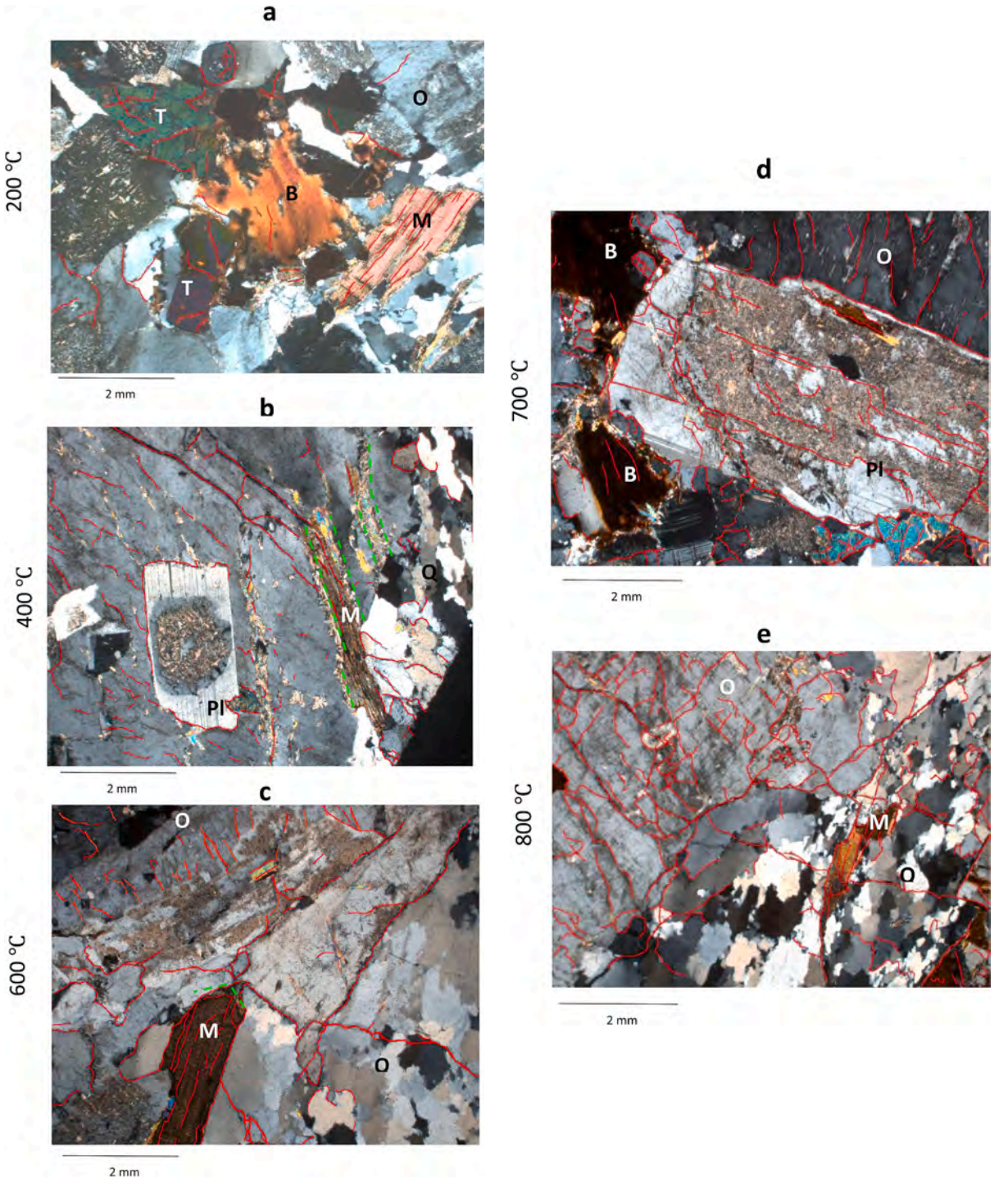


**Fig. 6.** Cross polarized 5 mm field of view images of thermally treated Devon Granite from 200 to 800 °*C* (a–e) showing progressive fracturing (Red) & degradation of the granite with temperature. This includes continuous quartz sub grain development (Q), development of fine-grained muscovite fringes (Green). The figure also shows progressive fracturing along cleavage planes and grain boundaries of feldspar and muscovite, plagioclase (Pl) and tourmaline (T) grains. Fracturing was also seen to mimic perthites in orthoclase (O) and at high temperatures cross randomly through quartz grains. Gradual oxidation of biotite mica (B) is also observed as thermal treatment temperature increases. (For interpretation of the references to colour in this figure legend, the reader is referred to the Web version of this article.)

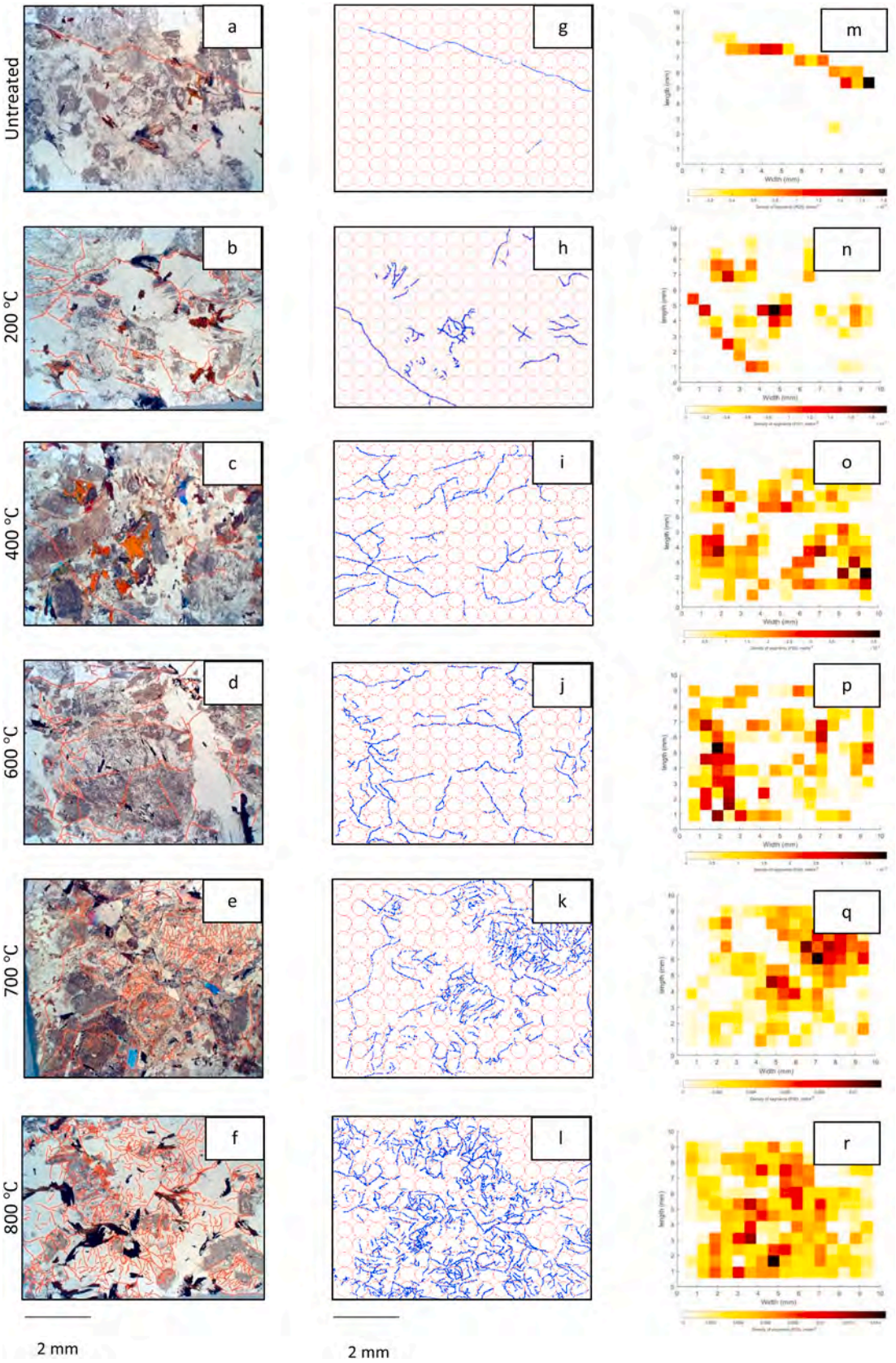


*(caption on next page)*

**Fig. 7.** Procedure of using FracPaQ. Fractures (marked in red) are drawn over thin section images of the thermally treated granite (a–f). Fractures are then subsequently processed in FracPaQ via circular scanline sampling (g–k) to isolate fracture segments, marked in blue (g–l). Fracture density images are then produced in FracPaQ (m–r) to quantify fracture distribution. (For interpretation of the references to colour in this figure legend, the reader is referred to the Web version of this article.)

from Devon, southwest England. At temperatures up to 500 °C it is straightforward to use the Griffith fracture criterion for the influence of applied thermal stress of overall mechanical strength [32]. The primary mechanism taking place is thermal expansion, resulting in stress concentrations at grain boundaries, and nucleation of microfracturing from pre-existing fractures [23]. Evidence for microfracture nucleation was observed in thin section at 200 °C with microfractures passing from one quartz grain to another and connecting with the boundaries of neighbouring K-feldspar crystals. At 400 °C the nucleation of fractures increased around quartz sub-grain boundaries with evidence of thermal expansion as micas became deformed and with obvious fine-grained fringes [36–38]. Thermal expansion is also likely to make basal cleavages more noticeable (Fig. 6a and b) and promote fracture growth along pre-existing microfractures, chemical zoning and planes of weakness [39–42]. The thermal energy used to break those bonds is likely to be dissipated into the surrounding groundmass and to grains in closest proximity, thus favouring the formation of intergranular cracks with respect to intragranular cracks at lower temperatures. This is what was observed in thin section (Fig. 6a) and empirically where the number of intergranular segments, the average intergranular segment length and intergranular fracture density, was higher than intragranular fractures. Furthermore, this was observed in alkali feldspars (Fig. 6b and c) at 400 °C and 600 °C, with fractures mimicking cleavage planes. Microfracturing was also observed in the fresher areas of otherwise sericitized zones in plagioclase feldspars (Fig. 6 and d). Microscopic observation reveals that the application of increasing thermal treatment has led to the formation of a distinct interconnecting fracture network from the untreated granite by 700–800 °C (Fig. 6d and e) where fractures further developed along predetermined structural planes, such as twinning in plagioclase and cleavage in muscovite. The process of fracture nucleation with increasing temperature has been aided by pre-existing fractures along cleavages and grain boundaries (Fig. 1). These features acted as stress concentrators resulting in the distribution of fractures throughout the rock fabric.

The effects of the microstructural changes are very clearly seen in both elastic wave and mechanical data. Crack porosity increases by just under 0.5%, but P-wave velocity decreases significantly from 4.71 km/s to 3.74 km/s. This disproportional effect of fractures on elastic wave velocity is well reported [8,14,24]. It is likely that the change in porosity at low temperatures is a result of the competition between pre-existing and newly-forming fractures, limiting the overall fracture damage. However, beyond 400 °C , further fracture damage occurs, leading to significant changes in density, porosity and tensile strength. At 573 °C, because of the $\alpha - \beta$ phase transition of quartz, which causes sudden volume changes, a significant increase in fracture damage is observed in our data, consistent with earlier work [43–47]. Thin section analysis from 600 °C on treated samples (Fig. 6d) illustrate these effects, including an increase in straining within quartz grains, microfractures passing through quartz grains and interacting with K-feldspar and plagioclase feldspars across the margins of grain boundaries. In contrast, tensile strength gradually decreased from untreated to 400 °C as thermal expansion took place. However, after the $\alpha - \beta$ phase transition, the tensile strength of the granite decreases to and remains between 2 and 3 MPa. The phase transition temperature also marks where intergranular and intragranular fracture density steadily increased to 2 $mm^{-2}$ with increasing temperature up to 800 °C (Fig. 11). These results can be attributed to the weakening of grain boundary strength at high temperatures [48]. Grain boundary fractures are almost fully developed at 500 °C and subsequently allow the rapid initialisation of intragranular fracturing (Fig. 9) [48]. This phenomena would lead to grain decohesion and dislocation in all treatment cycles that extended beyond the $\alpha - \beta$ phase transition, without significant variation of fracture connectivity, which suggests why the tensile strength remained below 3 MPa.

We observe a significant decrease in P- wave velocity occurring at approximately at 600 °C, which may be linked changes to the $\alpha - \beta$ phase transition in quartz [49,50]. However, in our data we note the greatest decrease in P-wave velocity between 700 °C and 800 °C [19,51]. This may be due to post-transitional growth of fractures that had already formed during the $\alpha - \beta$ phase transition, combined with additional deformation of muscovite mica (Fig. 6b, c and d), which we see here to have become more bent and kinked. In addition, tourmaline crystals are heavily fractured (Fig. 6e), resulting in increasing values of fracture segments (Fig. 9) and fracture density (Fig. 10) with increasing thermal stressing temperature [47]. As a result, the structural integrity of the granite has been greatly reduced so that beyond 700 °C, the ability for the granite to withstand further damage is limited leading to more significant decreases in P-wave velocity [52].

A link between fracture density and elastic wave velocity can be established using the method of Nasseri et al. [11] which allows direct comparison between optical image data and the measured P-wave elastic data. Using (1) [11] we define fracture density $\rho_c$ as:

$$\rho_c = \frac{1}{V}\sum_{i=1}^{N} c_i^3 \tag{1}$$

where $c_i^3$ is the radius of the ith crack and $N$ is the total number of cracks in the representative volume $V$. This definition is then used to calculate the Youngs Modulus, $E^*$, and from that, the elastic P-wave velocity, $v_p$ via the following two relationships:

$$\frac{E_0}{E^*} = 1 + \frac{16\left(1 - a_0^2\right)\left(1 - \frac{3a_0}{10}\right)}{9\left(1\frac{a_0}{2}\right)}\rho_c \tag{2}$$

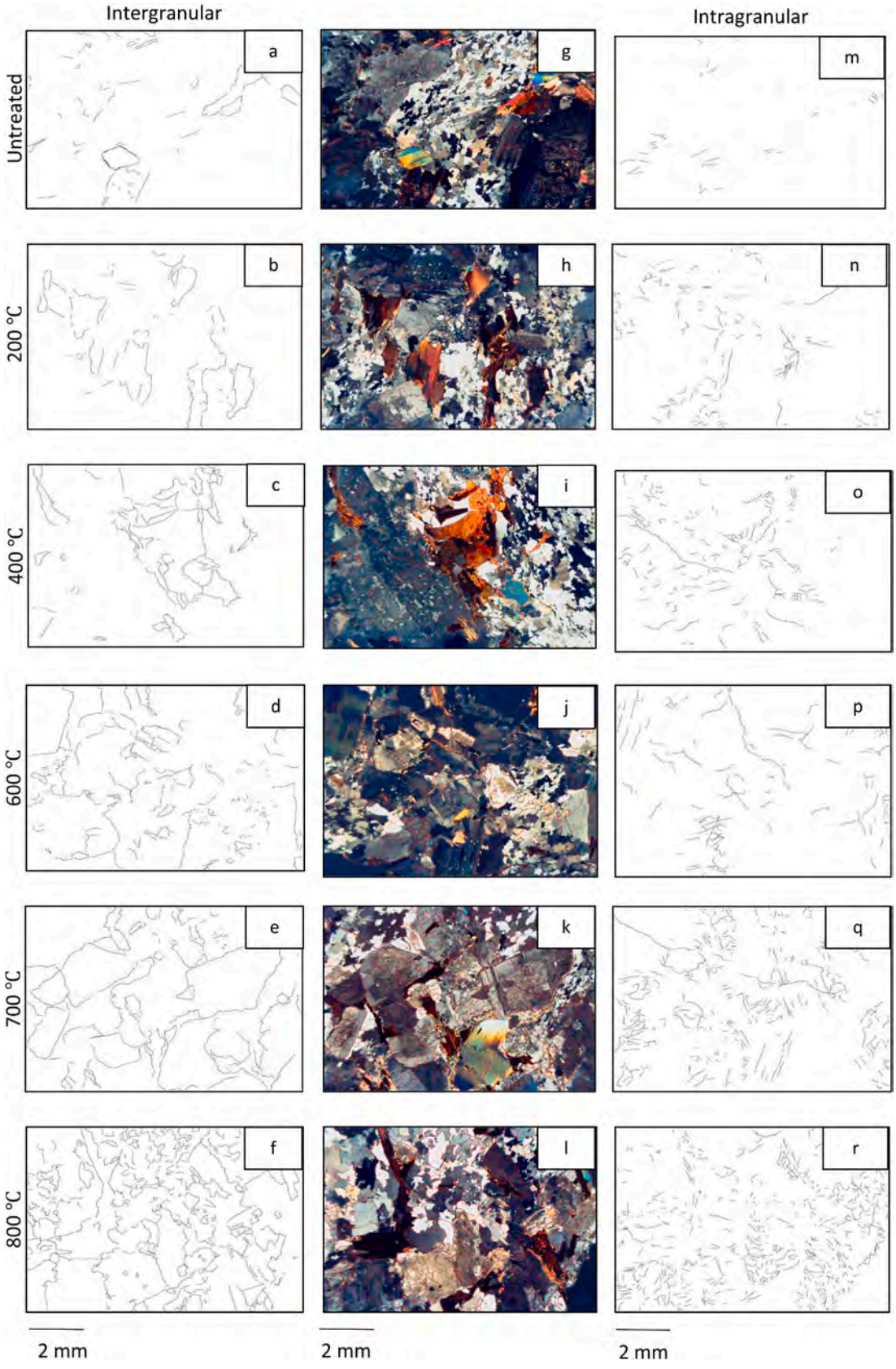


(caption on next page)

**Fig. 8.** Evolution of Intergranular (a–f) and intragranular (m–r) fracturing that has taken place in the granite during the thermal treatment process (g–l).

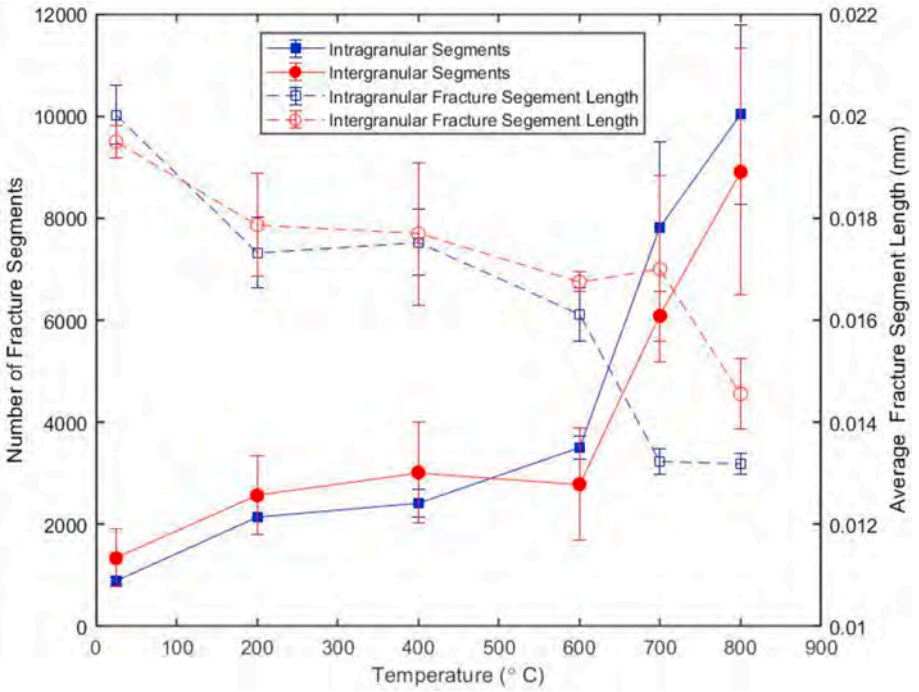


**Fig. 9.** Comparison of the number of intergranular and intragranular fracture segments and average length of Intergranular and Intragranular fracture segments from circular scanline sampling in FracPaQ.

**Table 4**
Intergranular and Intragranular fracture data from FracPaQ.

| Temperature °C | No. Fracture Segments | | Average Segment Length (mm) | | Average Fracture Density ($mm^{-2}$) | |
|---|---|---|---|---|---|---|
| | Intergranular | Intragranular | Intergranular | Intragranular | Intergranular | Intragranular |
| 25 | 1228 | 889 | 0.019 | 0.019 | 0.24 | 0.18 |
| 200 | 2570 | 2147 | 0.018 | 0.017 | 0.51 | 0.5 |
| 400 | 3017 | 2416 | 0.018 | 0.018 | 0.6 | 0.42 |
| 600 | 2789 | 3500 | 0.017 | 0.016 | 0.55 | 0.69 |
| 700 | 6085 | 7820 | 0.015 | 0.013 | 0.89 | 1.55 |
| 800 | 8905 | 10,030 | 0.015 | 0.013 | 1.77 | 1.99 |

$$v_p = \sqrt{(E^*/\rho\left(\frac{(1-a_0)}{(1-2a_0)(1+a_0)}\right))} \tag{3}$$

where $E_0$ and $a_0$ are the Youngs modulus (75 MPa) and $a_0$ is the Poisson's ratio (0.2) of untreated Devon Granite, $\rho$ is the density of the core samples [11,53]. The relationships in (2) and (3) are then used to calculate the data in Table 5 below.

These numerically-derived elastic P-wave velocity values (Table 5) may be normalised and compared against normalised directly-measured P-wave velocity values (Fig. 12). Here we see that the numerical model reproduces the general behaviour of the laboratory measured P-wave velocity values with increasing temperature. The model slightly underestimates the decreasing P-wave velocity up to approximately 450 °C. It is likely that this is due to the directly measured fracture density underreporting smaller fractures, which are below the resolution that can be identified optically. However, past 500 °C the normalised values at 600 and 800 °C closely match the measured results. This suggests that the effect of the $\alpha - \beta$ phase transition has produced fractures that can be optically identified to determine fracture density for the thermally treated granite. This produces a model output that is a closer estimation for P-wave velocity as derived from microfractures. The development of microfracturing along cleavage planes in muscovite and twinning in plagioclase at high temperatures may also have influenced fracturing, leading to lower P-wave velocity results which are particularly sensitive to the presence of microfractures [54–56]. This hypothesis is supported by analysing the fracture data from thin section observations (Fig. 11), which show a rapid increase at around 600 °C in the density of intergranular and intragranular fractures, but without a direct correlation to the macroscopic (bulk) mechanical response exemplified by tensile strength.

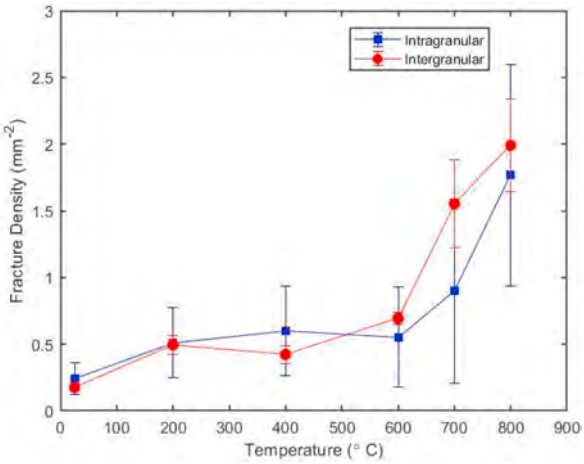


**Fig. 10.** Evolution of Intergranular and intragranular fracture density of thermally treated Devon granite calculated via FracPaQ.

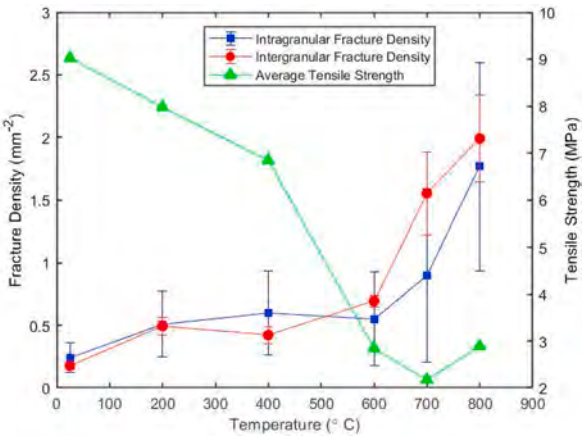


**Fig. 11.** Direct comparison of intergranular and intragranular fracture density and tensile strength of thermally treated Devon granite.

**Table 5**
Numerically derived P-wave velocity values.

| Temperature °C | Numerically Derived P-wave Velocity (km/s) |
|---|---|
| 25 | 3.81 |
| 200 | 3.44 |
| 400 | 3.36 |
| 600 | 3.28 |
| 700 | 2.68 |
| 800 | 2.46 |

## 5. Conclusions

The tensile strength of a collection of 10 coarse-grained granite samples sourced from the Cornubian Batholith in Devon, southwest England has been tested after being thermally treated to increasing temperatures up to 800 °C. The effect of temperature on the samples has been evaluated by integrating experimental physical parameters such as density, porosity and P-wave velocity with fracture density obtained by the FracPaQ toolbox. Theoretical inversions of the physical properties have been subsequently calculated to assess quantitatively the extent of fracture density. Such an integration of rock physics data has been combined with a detailed and extensive petrological study to cross-reference the mechanical effects of intergranular and intergranular fracturing to the overall macroscopic behaviour of the granite.

Taking the additional information from the petrology and image analysis into account, we conclude that mineral structures such as cleavage and twinning significantly influence intergranular and intragranular fracturing. The fracturing is particularly sensitive to P-

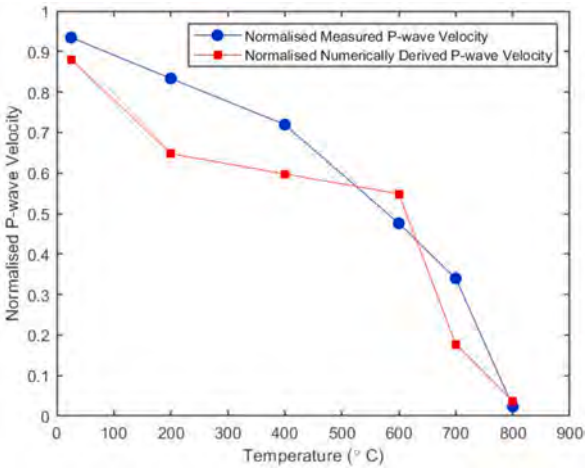


**Fig. 12.** Normalised comparison between laboratory measured P-wave velocity and a numerically derived P-wave velocity that incorporates fracture density values generated through FracPaQ.

wave elastic velocity compared to macroscopic properties such as tensile strength. Using images of thermally stressed granite via the FracPaQ toolbox, we found that intergranular and intragranular fracture density increased with thermal treatment temperature, while fracture segment length decreased.

We further conclude that the increase of thermal treatment temperature had a significant impact on the macroscopic behaviour of the granite samples, including tensile strength which decreased from 9 MPa to 3 MPa, consistently with previous work. A numerical P-wave velocity, calculated from a static Youngs modulus derived from optical fracture density using FracPaQ, has been compared to laboratory P-wave velocity. The data sets show a similar behaviour to one another with increasing thermal stressing temperature suggesting that the analysis of images via the FracPaQ toolbox is an effective tool at simulating laboratory observations. Taken together, it is likely that micro-scale features may be used as a reasonable proxy for macro-scale strength and mechanical data for materials dominated by fracture damage.

## Author contribution statement

Thomas Alcock: Conceived and designed the experiments; Performed the experiments; Analyzed and interpreted the data; Wrote the paper.

Dean Bullen: Analyzed and interpreted the data; Wrote the paper.

Phil Benson, Sergio Vinciguerra: Conceived and designed the experiments; Analyzed and interpreted the data; Contributed reagents, materials, analysis tools or data; Wrote the paper.

## Funding statement

This research did not receive any specific grant from funding agencies in the public, commercial, or not-for-profit sectors.

## Data availability statement

Data will be made available on request.

## Declaration of interest's statement

The authors declare no competing interests.

## References

[1] D. McKenzie, N. Weiss, Speculations on the thermal and tectonic history of the Earth, Geophys. J. Roy. Astron. Soc. 42 (1) (1975) 131–174, https://doi.org/10.1111/j.1365-246X.1975.tb05855.x.

[2] P. Morgan, D.D. Blackwell, R.E. Spafford, R.B. Smith, Heat flow measurements in Yellowstone Lake and the thermal structure of the Yellowstone Caldera, J. Geophys. Res. 82 (26) (1977) 3719–3732.

[3] O.G. Flovenz, K. Saemundsson, Heat flow and geothermal processes in Iceland, Tectnophysics 225 (1–2) (1993) 123–138.

[4] P. England, M. Bickle, Continental thermal and tectonic regimes during the Archean, J. Geol. 92 (4) (1984) 353–367.

[5] K. Ágústsson, Ó.G. Flóvenz, The Thickness of the Seismogenic Crust in Iceland and its Implications for Geothermal, in: Proc World Geotherm Congr. 2005, vol. 2005, 2015, p. 9.

[6] P. Ledingham, L. Cotton, R. Law, The United Downs Deep Geothermal Power Project, in: Proc 44th Work Geotherm Reserv Eng. 2019, 1989, pp. 1–11. https://pangea.stanford.edu/ERE/db/GeoConf/papers/SGW/2019/Law.pdf.

[7] W. Yu, L. Bao-lin, Z. Hai-yan, Y. Chuan-liang, L. Zhi-jun, W. Zhi-qiao, Thermophysical and Mechanical Properties of Granite and its Effects on Borehole Stability in High Temperature and Three-Dimensional Stress. 2014, 2014.

[8] W. Zhang, Q. Sun, Y. Zhang, L. Xue, F. Kong, Porosity and wave velocity evolution of granite after high-temperature treatment: a review, Environ. Earth Sci. 77 (9) (2018) 1–13, https://doi.org/10.1007/s12665-018-7514-3.

[9] X.L. Xu, Z.-Z. Zhang, Acoustic emission and damage characteristics of granite subjected to high temperature, Adv. Mater. Sci. Eng. 2018 (2018) 1–12, https://doi.org/10.1155/2018/8149870.

[10] S. Vinciguerra, C. Trovato, P.G. Meredith, P.M. Benson, Relating seismic velocities , thermal cracking and permeability in Mt, Etna and Iceland Basalts 42 (2005) 900–910, https://doi.org/10.1016/j.ijrmms.2005.05.022.

[11] M.H.B. Nasseri, A. Schubnel, R.P. Young, Coupled evolutions of fracture toughness and elastic wave velocities at high crack density in thermally treated Westerly granite, Int. J. Rock Mech. Min. Sci. 44 (2007) 601–616, https://doi.org/10.1016/j.ijrmms.2006.09.008.

[12] A. Ronov, A. Yaroshevsky, Chemical Composition of the Earth's Crust, in: Washingt DC Am Geophys Union Geophys Monogr Ser., vol. 13, 1969, pp. 37–57.

[13] F. Wang, T. Frühwirt, H. Konietzky, Q. Zhu, Thermo-mechanical behaviour of granite during high-speed heating, Eng. Geol. 260 (August) (2019), 105258, https://doi.org/10.1016/j.enggeo.2019.105258.

[14] P. Wang, T. Yin, X. Li, S. Zhang, L. Bai, Dynamic properties of thermally treated granite subjected to cyclic impact loading, Rock Mech. Rock Eng. 52 (4) (2019) 991–1010, https://doi.org/10.1007/s00603-018-1606-y.

[15] P.K. Gautam, A.K. Verma, M.K. Jha, P. Sharma, T.N. Singh, Effect of high temperature on physical and mechanical properties of Jalore granite, J. Appl. Geophys. 159 (2018) 460–474, https://doi.org/10.1016/j.jappgeo.2018.07.018.

[16] L. Griffiths, M.J. Heap, P. Baud, J. Schmittbuhl, Quantification of microcrack characteristics and implications for stiffness and strength of granite, Int. J. Rock Mech. Min. Sci. 100 (2017), https://doi.org/10.1016/j.ijrmms.2017.10.013.

[17] Z. Zhao, Thermal influence on mechanical properties of granite: a microcracking perspective, Rock Mech. Rock Eng. 49 (3) (2016) 747–762, https://doi.org/10.1007/s00603-015-0767-1.

[18] W.G.P. Kumari, D.M. Beaumont, P.G. Ranjith, M.S.A. Perera, B.L. Avanthi Isaka, M. Khandelwal, An experimental study on tensile characteristics of granite rocks exposed to different high-temperature treatments, Geomech. Geophys. Geo-Energy Geo-Resour. 5 (1) (2019) 47–64, https://doi.org/10.1007/s40948-018-0098-2.

[19] M.H.B. Nasseri, B.S.A. Tatone, G. Grasselli, R.P. Young, Fracture toughness and fracture roughness interrelationship in thermally treated westerly granite, Pure Appl. Geophys. 166 (5–7) (2009) 801–822, https://doi.org/10.1007/s00024-009-0476-3.

[20] L. Griffiths, M.J. Heap, P. Baud, J. Schmittbuhl, Quantification of microcrack characteristics and implications for stiffness and strength of granite, Int. J. Rock Mech. Min. Sci. 100 (October) (2017) 138–150, https://doi.org/10.1016/j.ijrmms.2017.10.013.

[21] S. Chen, C. Yang, G. Wang, Evolution of thermal damage and permeability of Beishan granite, Appl. Therm. Eng. 110 (2017) 1533–1542, https://doi.org/10.1016/j.applthermaleng.2016.09.075.

[22] J.T. Fredrich, T.F. Wong, Micromechanics of thermally induced cracking in three crustal rocks, J. Geophys. Res. 91 (B12) (1986) 12743–12764.

[23] W. Lin, Permanent strain of thermal expansion and thermally induced microcracking in Inada granite, J. Geophys. Res. Solid Earth 107 (B10) (2002), https://doi.org/10.1029/2001jb000648. ECV 3-1-ECV 3-16.

[24] Y.L. Chen, S.R. Wang, J. Ni, R. Azzam, T.M. Fernández-steeger, An experimental study of the mechanical properties of granite after high temperature exposure based on mineral characteristics, Eng. Geol. 220 (2017) 234–242, https://doi.org/10.1016/j.enggeo.2017.02.010.

[25] D. Healy, R.E. Rizzo, D.G. Cornwell, et al., FracPaQ: a MATLAB$^{TM}$ toolbox for the quantification of fracture patterns, J. Struct. Geol. 95 (2017) 1–16, https://doi.org/10.1016/j.jsg.2016.12.003.

[26] A. Brammall, H.F. Harwood, The Dartmoor granite : its mineralogy, structure, and petrology, J. Minerol. Soc. Minerol. Soc. 20 (101) (1923) 49–70.

[27] B.W. Chappell, R. Hine, The Cornubian Batholith: an example of magmatic fractionation on a crustal scale, Resour. Geol. 56 (3) (2006) 203–244, https://doi.org/10.1111/j.1751-3928.2006.tb00281.x.

[28] A. Castagna, A. Ougier-Simonin, P.M. Benson, et al., Thermal damage and pore pressure effects of the brittle-ductile transition in Comiso limestone, J. Geophys. Res. Solid Earth 123 (9) (2018) 7644–7660, https://doi.org/10.1029/2017JB015105.

[29] G. Simmons, W.F. Brace, Comparison of static and dynamic measurements of compressibility of rocks, J. Geophys. Res. 70 (22) (1965) 5649–5656.

[30] ISRM, Suggested methods for determining the uniaxial compressive strength and deformability of rock materials, Int. J. Rock Mech. Min. Sci. 16 (2) (1979) 135–140.

[31] I.S.R.M. Suggested, Methods for determining tensile strength of rock materials Part 2: suggested method for determining indirect tensile strength by the Brazil test, Int. J. Rock Mech. Min. Sci. 15 (1978) 99–103.

[32] A.A. Griffits, The phenomena of rupture and flow in solids, Masinovedenie C (1) (1995) 9–14, https://doi.org/10.1098/rsta.1921.0006.

[33] M.D. Sangid, H.J. Maier, H. Sehitoglu, The role of grain boundaries on fatigue crack initiation - an energy approach, Int. J. Plast. 27 (5) (2011) 801–821, https://doi.org/10.1016/j.ijplas.2010.09.009.

[34] K. Tanaka, T. Mura, A dislocation model for fatigue crack initiation, J. Appl. Mech. 48 (1) (1981) 97–103.

[35] M. Mauldon, W.M. Dunne, M.B. Rohrbaugh, Circular scanlines and circular windows: new tools for characterizing the geometry of fracture traces, J. Struct. Geol. 23 (2–3) (2001) 247–258, https://doi.org/10.1016/S0191-8141(00)00094-8.

[36] R. Homand-Etienne, R. Houpert, Thermally induced microcracking in granites: characterization and analysis, Int. J. Rock Mech. Min. Sci. 26 (2) (1989) 125–134.

[37] S. Brantley, The effect of fluid chemistry on quartz microcrack lifetimes, Earth Planet Sci. Lett. 113 (1–2) (1992) 145–156.

[38] E. Eberhardt, B. Stimpson, D. Stead, The Influence of Mineralogy on the Initiation of Microfractures in Granite, in: Pap Present 9th ISRM Congr Paris, Fr, 1999. Published online.

[39] P. Vázquez, V. Shushakova, M. Gómez-Heras, Influence of mineralogy on granite decay induced by temperature increase: experimental observations and stress simulation, Eng. Geol. 189 (2015) 58–67, https://doi.org/10.1016/j.enggeo.2015.01.026.

[40] A. Shyam, E. Lara-Curzio, A. Pandey, T.R. Watkins, K.L. More, The thermal expansion, elastic and fracture properties of porous cordierite at elevated temperatures, J. Am. Ceram. Soc. 95 (5) (2012) 1682–1691, https://doi.org/10.1111/j.1551-2916.2012.05125.x.

[41] D.M. Freire-Lista, L.S. Gomez-Villalba, R. Fort, Microcracking of granite feldspar during thermal artificial processes, Period. Mineral. 84 (3A) (2015) 519–537, https://doi.org/10.2451/2015PM0029.

[42] H. Hu, S. Liu, H.R. Fan, K. Yang, Y. Zuo, Y. Cai, Structural networks Constraints on alteration and mineralization processes in the Jiaojia Gold Deposit, Jiaodong Peninsula, China, J. Earth Sci. 31 (3) (2020) 500–513, https://doi.org/10.1007/s12583-020-1276-z.

[43] H. Kern, Effect of high-low quartz transition on compressional and shear wave velocities in rocks under high pressure, Phys. Chem. Miner. 4 (1979) 161–171.

[44] M.I.J. Probert, An ab initio study of xenon retention in α-quartz, J. Phys. Condens. Matter 22 (2) (2010), https://doi.org/10.1088/0953-8984/22/2/025501.

[45] H. Kimizuka, H. Kaburaki, Y. Kogure, Molecular-dynamics study of the high-temperature elasticity of quartz above the α-β phase transition, Phys. Rev. B Condens. Matter 67 (2) (2003) 1–7, https://doi.org/10.1103/PhysRevB.67.024105.

[46] M. Hajpál, Á. Török, Mineralogical and colour changes of quartz sandstones by heat, Environ. Geol. 46 (3–4) (2004) 311–322, https://doi.org/10.1007/s00254-004-1034-z.

[47] A.S. Zappone, P.M. Benson, Effect of phase transitions on seismic properties of metapelites: a new high-temperature laboratory calibration, Geology 41 (4) (2013) 463–466, https://doi.org/10.1130/G33713.1.

[48] J. Wang, J. Zuo, Y. Sun, J. Wen, The effects of thermal treatments on the fatigue crack growth of Beishan granite: an in situ observation study, Bull. Eng. Geol. Environ. 80 (2) (2021) 1541–1555, https://doi.org/10.1007/s10064-020-01966-w.

[49] R.D. Dwivedi, Prasad VVR. Goel, A. Sinha, Thermo-mechanical properties of Indian and other granites, Geothermics 44 (3) (2017) 1–11, https://doi.org/10.1016/j.geothermics.2014.11.005.
[50] T. Yin, X. Li, W. Cao, K. Xia, Effects of thermal treatment on tensile strength of laurentian granite using Brazilian test, Rock Mech. Rock Eng. 48 (6) (2015) 2213–2223, https://doi.org/10.1007/s00603-015-0712-3.
[51] P. Jin, Y. Hu, J. Shao, G. Zhao, X. Zhu, C. Li, Influence of different thermal cycling treatments on the physical, mechanical and transport properties of granite, Geothermics 78 (January) (2019) 118–128, https://doi.org/10.1016/j.geothermics.2018.12.008.
[52] T. Yin, L. Bai, X. Li, X. Li, S. Zhang, Effect of thermal treatment on the mode I fracture toughness of granite under dynamic and static coupling load, Eng. Fract. Mech. 199 (May) (2018) 143–158, https://doi.org/10.1016/j.engfracmech.2018.05.035.
[53] R. Parker, Hot dry rock geothermal energy research at the Camborne School of, Mines, Bull. Geoth. Resour. Counc. 18 (9) (1989) 3–7.
[54] E. Mariani, K.H. Brodie, E.H. Rutter, Experimental deformation of muscovite shear zones at high temperatures under hydrothermal conditions and the strength of phyllosilicate-bearing faults in nature, J. Struct. Geol. 28 (9) (2006) 1569–1587, https://doi.org/10.1016/j.jsg.2006.06.009.
[55] S. Incel, J. Renner, B. Jamtveit, Evolution of brittle structures in plagioclase-rich Rocks.pdf, Geochem., Geophys. Geosyst. (21) (2020).
[56] T. Lokajíček, R. Vasin, T. Svitek, et al., Intrinsic elastic anisotropy of westerly granite observed by ultrasound measurements, microstructural investigations, and neutron diffraction, J. Geophys. Res. Solid Earth 126 (1) (2021) 1–23, https://doi.org/10.1029/2020JB020878.